ORIGINAL PAPER

Determination of cooling rates of glasses over four orders of magnitude

Alex Scarani[1] · Alessandro Vona[1] · Danilo Di Genova[2] · Raschid Al-Mukadam[3] · Claudia Romano[1] · Joachim Deubener[3]

Abstract

Volcanic materials can experience up to eleven orders of magnitude of cooling rate (q_c) starting from 10^{-5} K s^{-1}. The glassy component of volcanic material is routinely measured via differential scanning calorimeter (DSC) to obtain q_c through the determination of the glass fictive temperature (T_f). Conventional DSC (C-DSC), which has been employed for decades, can only access a relatively small range of q_c (from $\sim 10^{-2}$ to ~ 1 K s^{-1}). Therefore, extrapolations up to six orders of magnitude of C-DSC data are necessary to derive q_c of glasses quenched both at extremely low and high q_c. Here, we test the reliability of such extrapolations by combining C-DSC with the recently introduced flash calorimetry (F-DSC). F-DSC enables to extend the q_c exploration up to 10^4 K s^{-1}. We use three synthetic glasses as analogs of volcanic melts. We first apply a normalization procedure of heat flow data for both C-DSC and F-DSC to derive T_f as a function of experimental q_c, following the "unified area-matching" approach. The obtained T_f–q_c relationship shows that Arrhenius models, widely adopted in previous studies, are only valid for q_c determination within the calibration range. In contrast, a non-Arrhenius model better captures q_c values, especially when a significant extrapolation is required. We, therefore, present a practical "how-to" protocol for estimating q_c using DSC.

Keywords Glass · Differential scanning calorimetry · Cooling rate · Viscosity · Parallel shift factor

Introduction

Motivation and aims

The estimation of the cooling rate (q_c) embedded in volcanic glasses is pivotal for the reconstruction of their petrogenesis (Wilding et al. 1995, 1996a, b, 2000, 2004; Gottsmann and Dingwell 2001a, b, 2002; Gottsmann et al. 2004; Potuzak

Communicated by Mark S Ghiorso.

✉ Alex Scarani
   alex.scarani@uniroma3.it

1   Dipartimento di Scienze, Università degli Studi Roma Tre, Largo San L, Murialdo 1, 00146 Rome, Italy

2   Bavarian Research Institute of Experimental Geochemistry and Geophysics (BGI), University of Bayreuth, Universitätsstraße 30, 95440 Bayreuth, Germany

3   Institute of Non-Metallic Materials, Clausthal University of Technology, Zehntnerstraße 2a, 38678 Clausthal-Zellerfeld, Germany

et al. 2008; Nickols et al. 2009; Kueppers et al. 2012; Helo et al. 2013; Lavallée et al. 2015; Hui et al. 2018). Indeed, the q_c experienced by the magma controls the texture of volcanic rocks via the modulation of crystal and bubble growth with time, as well as the timescale of post-depositional processes such as sintering, welding, agglutination, rheomorphism, degassing, and crystallization (Quane et al. 2009; Shea et al. 2010; Gonnermann and Manga 2012; Di Genova et al. 2013; Vasseur et al. 2013; Vetere et al. 2015; Iezzi et al. 2017; Wadsworth et al. 2019; Cashman 2020; Giuliani et al. 2020; Di Fiore et al. 2021).

Here we present a combined conventional and flash differential scanning calorimetry (C-DSC and F-DSC) calibration by subjecting for the first time silicate melts of interest for volcanic processes to q_c ranging between 0.08 and 30,000 K s^{-1}. We significantly exceed the interval of q_c previously investigated in geospeedometry studies ($\sim 10^{-2}$ to ~ 1 K s^{-1}) and hence explore the validity of previous extrapolations from the relatively slow experimental q_c to the realm (> 10 K s^{-1}) of the submarine and explosive volcanism (e.g., Potuzak et al. 2008; Nickols et al. 2009). Our study is also of particular interest for

those melts prone to crystallization and dehydration during C-DSC measurements (Richet et al. 1996; Liebske et al. 2003; Di Genova et al. 2020a). Finally, we provide a practical "how-to" guide to calculating the cooling rate of volcanic glasses.

Theoretical background and experimental challenges

Two approaches are commonly employed to estimate q_c of the glass: (i) the first relies on the quantification of the molecular H_2O and OH^- species in the glass (Zhang et al. 1997, 2000; Benne and Behrens 2003; Behrens and Nowak 2003; Bauer et al. 2015; Behrens 2020) and requires knowledge of the chemical dependence of the absorption coefficients (e.g., Behrens 2020), whereas (ii) the second requires the knowledge of the limiting fictive temperature [T_f, Tool (1946)] of the glass and can be applied both on dry and hydrous glasses. Here, we focus on the latter method that lies at the heart of the enthalpy relaxation of the melt (Wilding et al. 1995, 1996a, b, 2000, 2004; Gottsmann and Dingwell 2001a, b, 2002; Potuzak et al. 2008; Nichols et al. 2009; Helo et al. 2013; Hui et al. 2018).

The enthalpy relaxation approach is based on the observation that the glass structure depends on the cooling rate at which the parental melt crossed the glass transition interval (Tool and Eichlin 1931; DeBolt et al. 1976; Moynihan et al. 1976). Once the transition is crossed, the melt structure appears frozen at the observation timescale. The glass retains the structure and properties (e.g., enthalpy, H, and volume, V) of the melt at the characteristic limiting fictive temperature, T_f (Tool 1946).

Because T_f correlates positively with q_c (e.g., Tool 1946; Moynihan et al. 1976), the knowledge of T_f enables the derivation of q_c, provided that the T_f vs. q_c relationship is known (Zheng et al. 2019). The T_f vs. q_c relationship has been observed to be Arrhenian (i.e., linear in the $-log_{10}(q_c)$ vs. $1/T_f$ space) at T close to T_g (e.g., Webb et al. 1992; Knoche et al. 1994; Potuzak et al. 2008; Zheng et al. 2019), where T_g is defined as the temperature at which the shear viscosity (η) of the melt is 10^{12} Pa s:

$$\eta\left(T_g\right) = 10^{12} Pa\ s \tag{1}$$

The Arrhenius correlation between q_c and T_f is described by the Tool (1946) equation:

$$-log_{10}|q_c| = -log_{10}A_q + \frac{E_a^q}{2.303RT_f} \tag{2}$$

where A_q and E_a^q are fitting parameters describing the pre-exponential factor and the activation energy for structural relaxation, respectively, and R is the gas constant. E_a^q scales with the activation energy of viscous flow (E_a^η; Moynihan

et al. 1976, 1996) that, for a relatively small temperature range, can be also approximated as Arrhenian:

$$log_{10}\eta = log_{10}A_\eta + \frac{E_a^\eta}{2.303RT} \tag{3}$$

where A_η is the pre-exponential factor corresponding to the viscosity at infinite T (Russell et al. 2003).

However, both descriptions of q_c (Eq. 2) and η (Eq. 3) are non-Arrhenian when considered across the whole T range of silicate melts (Angell 1985; Hui and Zhang 2007; Giordano et al. 2008; Mauro et al. 2009; Zheng et al. 2017). The degree of deviation from the Arrhenian behavior can be described by the fragility index m_{vis}, also known as kinetic melt fragility:

$$m_{vis} \equiv \left. \frac{\partial log_{10}\eta}{\partial T_g/T} \right|_{T=T_g} \tag{4}$$

Similarly, the degree of deviation from the Arrhenian behavior for q_c follows the Moynihan et al. (1996) formulation:

$$m_{DSC} = -\frac{E_a^q}{2.303RT_g} \tag{5}$$

Zheng et al. (2017) found that m_{vis} correlates linearly and positively with the calorimetric fragility (m_{DSC}) over a wide range of kinetic fragility (varying from 26 to 108).

Different approaches have been proposed to derive T_f of glasses. One is the Tool-Narayanaswamy-Moynihan (TNM) enthalpy relaxation geospeedometer (e.g., Tool 1946; Narayanaswamy 1971, 1988; DeBolt et al. 1976; Moynihan et al. 1976; Wilding et al. 1995), whereas others belong to the "area-matching" (or "enthalpy-matching") methodologies (Moynihan et al. 1976; Yue et al. 2002; Potuzak et al. 2008; Nichols et al. 2009; Guo et al. 2011).

The TNM approach relates T_f to four parameters (A_q, E_a^q, β and ξ). It requires first multiple heat capacity measurements of the rejuvenated glass at different but matching cooling (DSC downscan) and heating (DSC upscan) cycles that allow the derivation of A_q and E_a^q (Eq. 2). Afterwards, two empirical parameters (β and ξ) ranging between 0 and 1 are fitted by tweaking them to minimize the root square mean error to derive T_f and thereby the unknown cooling rate (q_c). Kenderes and Whittington (2021) have recently provided a Matlab code to derive the four kinetic parameters without the need to perform multiple heat capacity measurements. However, the TNM approach cannot model the broad exothermic enthalpy relaxation upon DSC upscan before the glass transition interval typical of hyperquenched glasses (Yue et al. 2002; Potuzak et al. 2008; Nichols et al. 2009; Zheng et al. 2019).

The "area-matching" approaches offer a route to obtain T_f of glasses quenched at any cooling rate. These approaches are generally based on comparing two DSC upscans (see Zheng et al. 2019 for a review). Here the glass with unknown cooling rate is heated (upscan 1) above the glass transition interval until the liquid state (i.e., $T_f = T$) to erase its thermal history. Afterwards, the rejuvenated melt is cooled (q_c) across glass transition interval below T_f and finally heated up (upscan 2) at the same rate (q_h). Because here $q_c = q_h$, the onset of the calorimetric glass transition (T_{onset}, Al-Mukadam et al. 2020) corresponds to T_f (Moynihan et al. 1976; Sherer 1984; Moynihan 1993, 1995; Yue et al. 2004; Zheng et al. 2019; Di Genova et al. 2020a). T_{onset} corresponds to the temperature of the crossing point between the tangent to the heat flow curve of the glass and the tangent to the inflection point on the following increase in heat flow (see "Treatment of DSC measurements and T_f determination") (Al-Mukadam et al. 2020; Di Genova et al. 2020a; Stabile et al. 2021). Finally, upscan 1 and 2 are compared, and T_f of the upscan 1 is obtained by a geometric reconstruction. This routine was recently refined by Guo et al. (2011) in the "unified area-matching" approach (see also "Treatment of DSC measurements and T_f determination") for C-DSC measurements. However, this approach cannot be applied when the sample undergoes physicochemical modifications (degassing and/or crystallization) occurring in the glass transition interval during the upscan of a few K per minute typical of C-DSC (Richet et al. 1996; Liebske et al. 2003; Di Genova et al. 2020a). Although there are no studies of this effect, we hypothesize that modifications are particularly likely in iron-bearing samples prone to FeO nanocrystallization whose formation changes melt chemistry, increasing the melt relaxation time (Di Genova et al. 2017; 2020b). Therefore, the first aspect to be explored in this study is the applicability of the "unified area-matching" approach for calorimetric measurements performed with the new flash DSC (F-DSC, q_c up to 5×10^4 K s^{-1}) that nowadays allows the study of the relaxation processes of extremely depolymerized melts through the suppression of crystallization (Schawe and Hess 2019; Al-Mukadam et al. 2020, 2021a, b).

Cooling rates ranges of volcanic glasses and literature assumptions

Figure 1 shows a compilation of cooling rates of volcanic glasses derived by conventional Differential Scanning Calorimetry (C-DSC) measurements by both TNM and area matching approaches. These glasses experienced more than ten orders of magnitude of q_c ranging from $\sim 10^{-5}$ K s^{-1} (agglutinate/welded materials; Wilding et al. 1995, 1996b; Gottsmann and Dingwell 2001a, 2002) to $\sim 10^6$ K s^{-1} (explosive submarine products; Potuzak et al. 2008; Helo et al. 2013). Glasses from a large spectrum of volcanic environments (effusive, explosive, and extra-terrestrial) experienced intermediate q_c (Wilding et al. 1995, 1996a, b; Wilding et al. 2000; Gottsmann and Dingwell 2001a, b, 2002; Gottsmann et al. 2004; Wilding et al. 2004; Potuzak et al. 2008; Nickols et al. 2009; Kueppers et al. 2012; Helo et al. 2013; Lavallée et al. 2015; Hui et al. 2018).

Fig. 1 Compilation of C-DSC derived cooling rates of volcanic glasses from the literature, grouped according to the formation environment. Source of data: Wilding et al. (2000), Potuzak et al. (2008), Nichols et al. (2009), Kueppers et al. (2012), and Helo et al. (2013) for submarine quenched glass; Wilding et al. (1995, 1996b), Gottsmann and Dingwell (2001a, b, 2002), Gottsmann et al. (2004), and Lavallée et al. (2015) for subaerial quenched glass; Wilding et al. (2004) for subglacial quenched glass; Wilding et al. (1996a), and Hui et al. (2018) for extra-terrestrial quenched glass. The horizontal and colored areas represent the range of experimental cooling rates for C-DSC and F-DSC
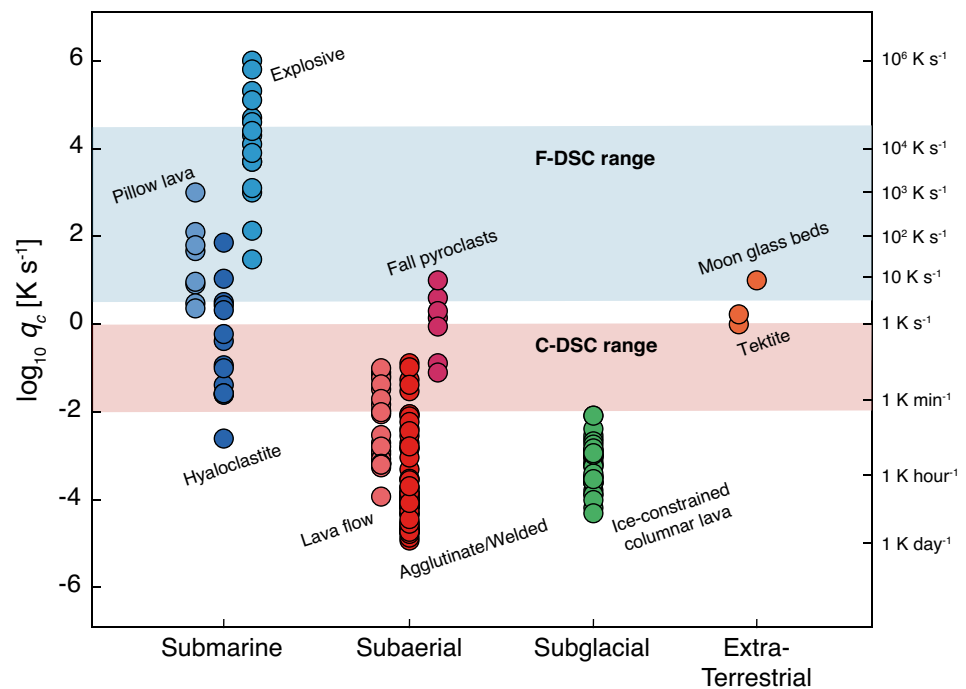
The accessible interval of $q_{c,h}$ of C-DSC equipment ranges from $\sim 10^{-2}$ to ~ 1 K s^{-1} (Wilding et al. 1995, 1996b; Gottsmann and Dingwell 2001a, 2002; Helo et al. 2013; Lavallée et al. 2015; Hui et al. 2018; Al-Mukadam et al. 2020; Fig. 1). Consequently, the T_f–q_c relationship calibration (Eq. 2) may require a significant Arrhenian extrapolation up to four orders of magnitude in the slow-cooling rate realm (e.g., agglutinated/welded pyroclasts), or even up to six orders of magnitude for the explosive submarine environment. Although this assumption may hold for nearly Arrhenian melts (i.e., "strong" melts after Angell 1985) where m_{vis} (Eq. 4) is ~ 15, the increase in melt fragility questions the reliability of cooling rate estimates through the Arrhenian extrapolation of Eq. 2.

As such, the second aspect to be explored in this study is the use of the F-DSC by subjecting glasses to high cooling rates and thus avoiding the extrapolation of C-DSC data to q_c typical of the submarine and the subaerial explosive environments (Fig. 1). The significant q_c expansion enables us to compare Arrhenian and non-Arrhenian models to describe the T_f–q_c relation, within and outside the calibration range.

Starting materials, experimental and analytical methods

Starting materials and their properties

We use three glasses: a sodium-calcium silicate (DGG-1, Meerlender 1974), a diopside (Di, Fanara and Behrens 2011), and a fluorophosphate (N-PK52A, Schott 2015). The chemical composition of the samples is listed in Table 1. The viscosity (Fig. 2a) and melt fragility (Fig. 2b) of these systems were characterized by Al-Mukadam et al. (2020). The melt fragility (m_{vis}) of our samples ranges from 37.8 (DGG-1) to 72.3 (N-PK52A), with the Di sample having $m_{vis} = 62.7$. Both the viscosity–temperature space and melt fragility of our melts well match the spectrum of viscosity and fragility of anhydrous and hydrous volcanic melts (shaded areas in Fig. 2) recently compiled by Langhammer et al. (2021).

The non-Arrhenian temperature dependence of viscosity (Fig. 2a) is described by VFT equations (Vogel 1921; Fulcher 1925; Tamman and Hesse 1926):

$$log_{10}\eta = A + \frac{B}{T(K) - C} \tag{6}$$

where A, B, and C are fitting parameters provided by Meerlender (1974) for DGG-1, by Reinsch et al. (2008) for Di, and by fitting viscometry data from Al-Mukadam et al. (2020) for N-PK52A (Supplementary Table 2). N-PK52A sample shows the lowest viscosity independently on T

Table 1 Chemical composition (mol%) of the investigated glasses

| Glass	DGG–1	Di	N–PK52A
Ref	Meerlender (1974)	Fanara and Behrens (2011)	Schott (2015) [in wt%]
SiO$_2$	70.9	49.9	–
TiO$_2$	0.1	–	–
Al$_2$O$_3$	0.7	–	10–20
FeO (T)	0.1	–	20–30
MnO	–	–	–
MgO	6.2	24.8	1–10
CaO	7.1	25.3	1–10
BaO	–	–	10–20
SrO	–	–	10–20
Na$_2$O	14.3	–	–
K$_2$O	0.2	–	–
Li$_2$O	–	–	–
P$_2$O$_5$	–	–	10–20
Nb$_2$O$_5$	–	–	<1
SO$_3$	0.3	–	–

See references for the errors in chemical analysis

(Fig. 2a). A crossover of viscosity is observed for DGG-1, and Di melts. The DGG-1 exhibits the higher viscosity only for T higher than 1334 K ($\sim 7.5 \times 10^4$ K^{-1} on the x-axis; Fig. 2a). This behavior results from the interplay between different melt fragility and T_g of the melts (Fig. 2b).

Differential scanning calorimetry

The T_f was determined by measuring the heat flow as a function of temperature using i) a C-DSC (404 F3 Pegasus) under N$_2$ 5.0 atmosphere (flow rate 30 ml min^{-1}) and ii) a F-DSC (Flash DSC 2+) equipped with the UFH 1 sensor, under constant gas flow (40 ml min^{-1}) of Ar 5.0. The C-DSC was calibrated using melting temperature and enthalpy of fusion of reference materials (pure metals of In, Sn, Bi, Zn, Al, Ag, and Au) up to 1337 K. The mass of the glasses measured with C-DSC was 28.20 mg for DGG-1, 22.90 mg for Di, and 26.60 mg for N-PK52A. The F-DSC was calibrated using the melting temperature of aluminum (melting temperature $T_m = 933.6$ K) and indium ($T_m = 429.8$ K). F-DSC measurements were conducted on glass chips with mass ranging from ~ 10 to ~ 300 ng depending on sample density (Al-Mukadam et al. 2020) to obtain an optimal signal-to-noise ratio.

For all measurements, 4 C-DSC and up to 14 F-DSC cycles of upscan and downscan were carried out at a fixed heating rate (q_h) and different cooling (q_c) rates. Heating rates imposed were ~ 0.17 K s^{-1} (10 K min^{-1}) and 1000 K s^{-1} (6×10^4 K min^{-1}) for C-DSC and F-DSC, respectively. Each
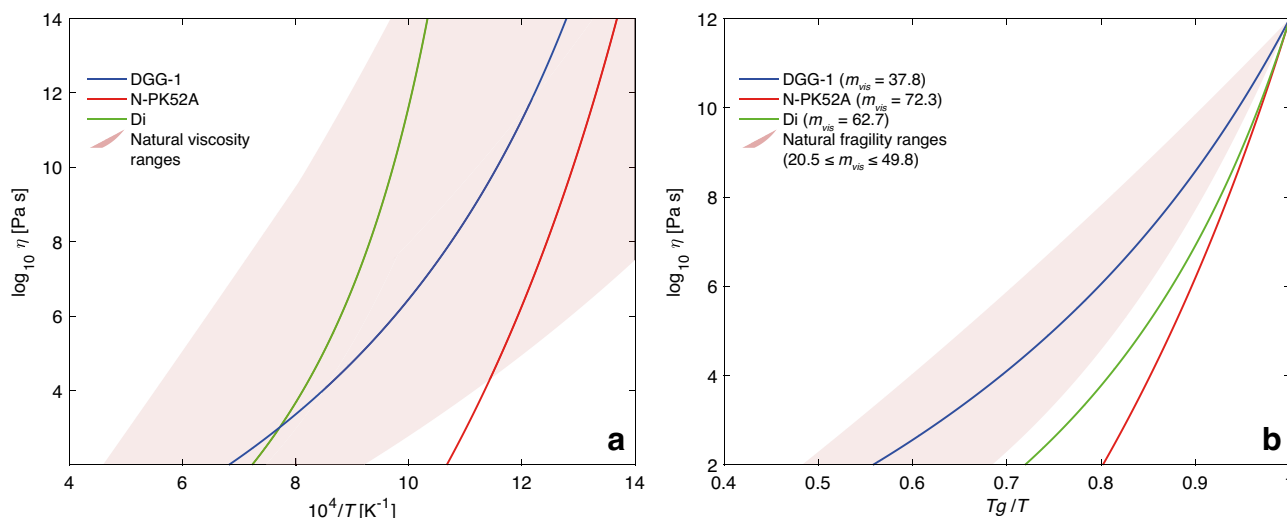
Fig. 2 **a** Viscosity of DGG-1, N-PK52A, and Di samples. The shaded area represents the viscosity spectrum of anhydrous and hydrous volcanic melts from Langhammer et al. (2021). **b** The Angell plot where the $log_{10}\eta$ of DGG-1, N-PK52A, and Di melts is plotted against the T_g-scaled inverse temperature. The shaded area represents the same plot for anhydrous and hydrous magmatic melts where m_{vis} ranges from 20.5 to 49.8 and T_g ranges from 814.7 to 1115.2 K (Langhammer et al. 2021). The fragility of our samples was estimated by Al-Mukadam et al. (2020)

upscan was followed by a downscan at a cooling rate ranging from ~0.08 to ~0.5 K s^{-1} (from 5 to 30 K min^{-1}) for C-DSC and from 3 to 30,000 K s^{-1} (from 180 to 1.8×10^6 K min^{-1}) for F-DSC. Consequently, one pair of upscan and downscan was performed at the same $q_{c,h}$ of ~0.17 K s^{-1} (10 K min^{-1}) and 1000 K s^{-1} for the C-DSC and F-DSC, respectively. We refer to this pair of scans as a "matching cycle".

Treatment of DSC measurements and T_f determination

The "unified area-matching" approach (Guo et al. 2011) for T_f determination requires baseline correction and normalization. Figure 3a, c, e shows the heat flow output of C-DSC. We derived the specific heat capacity (c_P in J g^{-1} K^{-1}) using a standard sapphire (21.21 mg; Archer 1993) (Potuzak et al. 2008; Nichols et al. 2009; Hui et al. 2018). The c_P error of the glassy contribution is $\pm 1\%$, whereas it is $\pm 3\%$ for the liquid state (e.g., Potuzak et al. 2008).

The glassy contribution (c_{Pg}) below the glass transition interval of matching cycles ($q_{c,h}$) at 10 K min^{-1} (black thick curves in Fig. 3a, c, e) was fitted using the Maier-Kelly empirical expression (Maier and Kelly 1932) to obtain the description of c_{Pg} also in the glass transition interval and liquid state. We first calculated the difference between c_P of the liquid state and c_{Pg} at T_{onset}, which here corresponds to T_f only for matching cycles ($q_{c,h} = 10$ K min^{-1} for C-DSC and 1000 K s^{-1} for F-DSCC) and specifically to T_g when $q_{c,h} = 10$ K min^{-1} (Moynihan et al. 1976; Sherer 1984; Moynihan 1993, 1995; Yue et al. 2004; Zheng et al.

2019; Stabile et al. 2021). This difference thus corresponds to the configuration heat capacity of the melt at T_g [$\Delta c_P (T_g)$] for C-DSC. We obtained $\Delta c_P (T_g)$ equal to 0.23 J g^{-1} K^{-1} for DGG-1, 0.45 J g^{-1} K^{-1} for Di, and 0.43 J g^{-1} K^{-1} for N-PK52A.

Subsequently, the Maier–Kelly fit of c_{Pg} was subtracted from all c_P measurements which were normalized using the $\Delta c_P (T_g)$ (Fig. 3b, d, f).

The procedure described so far was not applied to F-DSC measurements due to (1) the inability to acquire a proper background and sapphire measurements and (2) the extremely low sample mass (~10^{-8}–10^{-7} g) which would otherwise make the conversion of heat flow to heat capacity inaccurate (Schawe and Pogatscher 2016). Here we first applied a linear baseline over the heat flow of the glass region (Fig. 4a, c, e) and the heat flow data was subsequently converted to heat capacity (Fig. 4b, d, f) using $\Delta c_P (T_g)$ from C-DSC measurements (Fig. 3) after Schawe and Pogatscher (2016).

The fictive temperature T_f was estimated from the normalized c_P measurements. While $T_f \equiv T_{onset}$ for matching cycles (Fig. 5a), T_f of unmatching cycles was estimated according to the "unified area-matching" approach (Guo et al. 2011) as follows:

$$\int_{T_{onset}}^{T_f} (\Delta C_P) dT = \int_0^\infty (C_{P2} - C_{P1}) dT \tag{7}$$

where c_{P2} and c_{P1} are the normalized excess heat capacity of the matching and the unmatching cycle, respectively, and
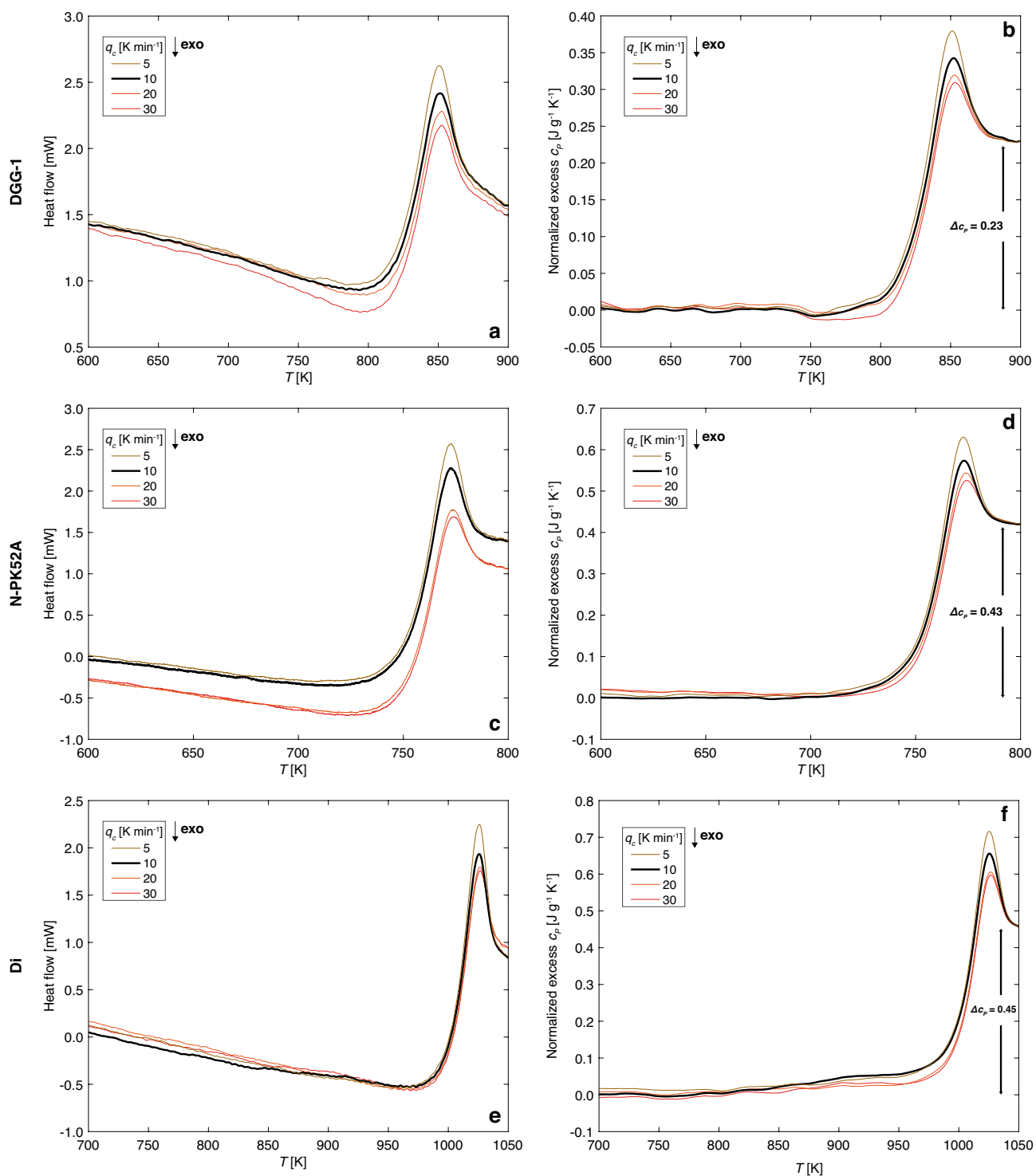
Fig. 3 C-DSC measurements (**a**, **c**, **e**) and treatment (**b**, **d**, **f**). Measured heat flow (**a**, **c**, **e**) and normalized excess c_P (**b**, **d**, **f**) of DGG-1, N-PK52A and Di samples measured at $q_h = 10$ K min^{-1} and variable q_c (from 5 to 30 K min^{-1}). The matching cycle at $q_{c,h} = 10$ K min^{-1} is shown as a thick black curve. Δc_P in panels **b**, **d**, **f** refers to to the configuration heat capacity of the melt at T_g (see text for details)
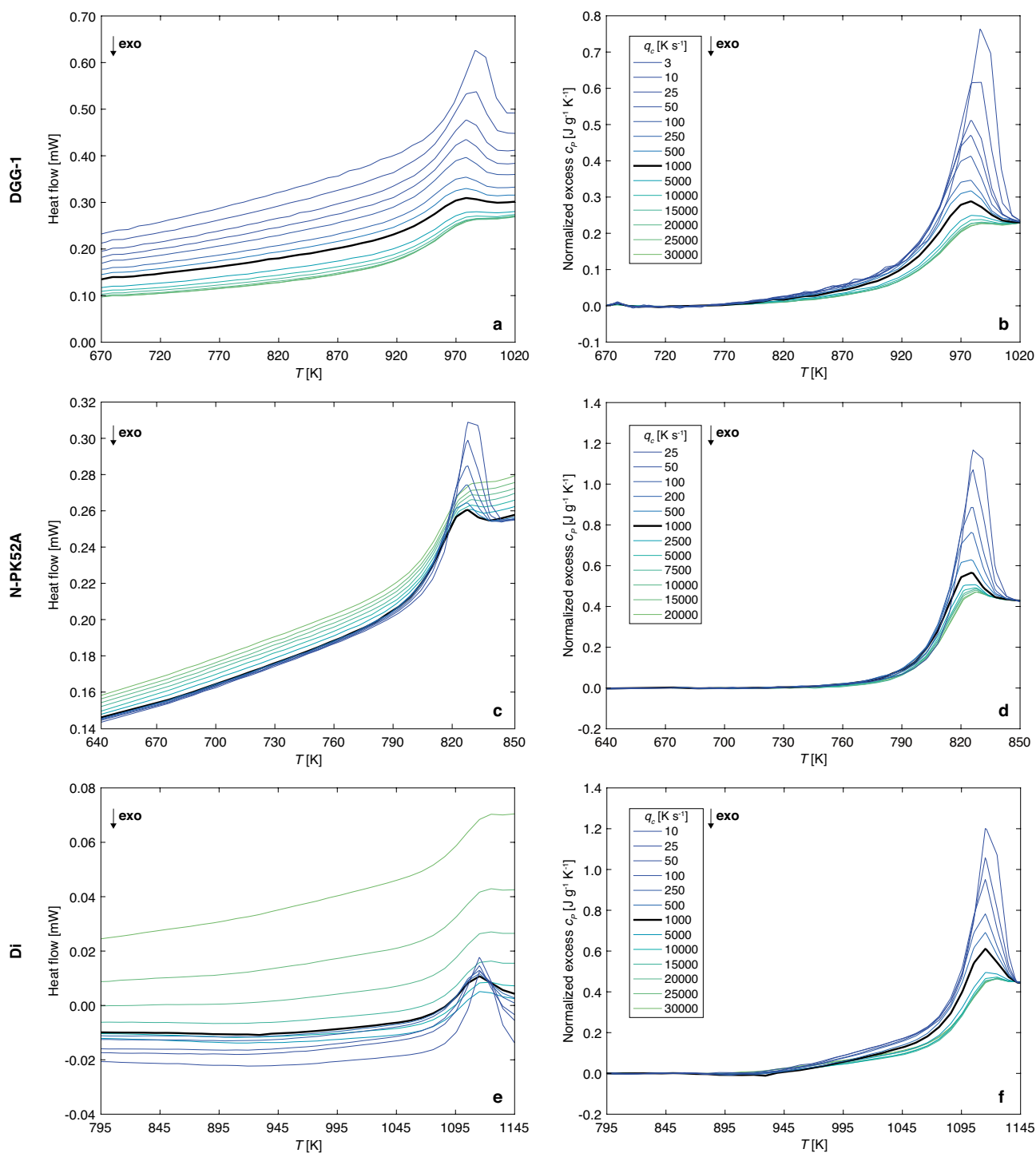
Fig. 4 C-DSC measurements (**a**, **c**, **e**) and treatment (**b**, **d**, **f**). Measured heat flow (**a**, **c**, **e**) and normalized excess c_P (**b**, **d**, **f**) of DGG-1, N-PK52A and Di samples at $q_h = 1000$ K s^{-1} and variable q_c (from 3

to 30,000 K s^{-1}). The matching cycle at $q_{c,h} = 1000$ K s^{-1} is showed as a thick black curve

Δc_P is the configurational heat capacity at T_g. The area difference between c_{P2} and c_{P1} corresponds to the rectangle whose base is defined by T_f–T_{onset} and height by Δc_P (Fig. 5b). T_f is thus the only unknown parameter.

Results

Al-Mukadam et al. (2020) determined the T_{onset} (i.e., T_f) via matching cycles over four orders of magnitude of $q_{c,h}$
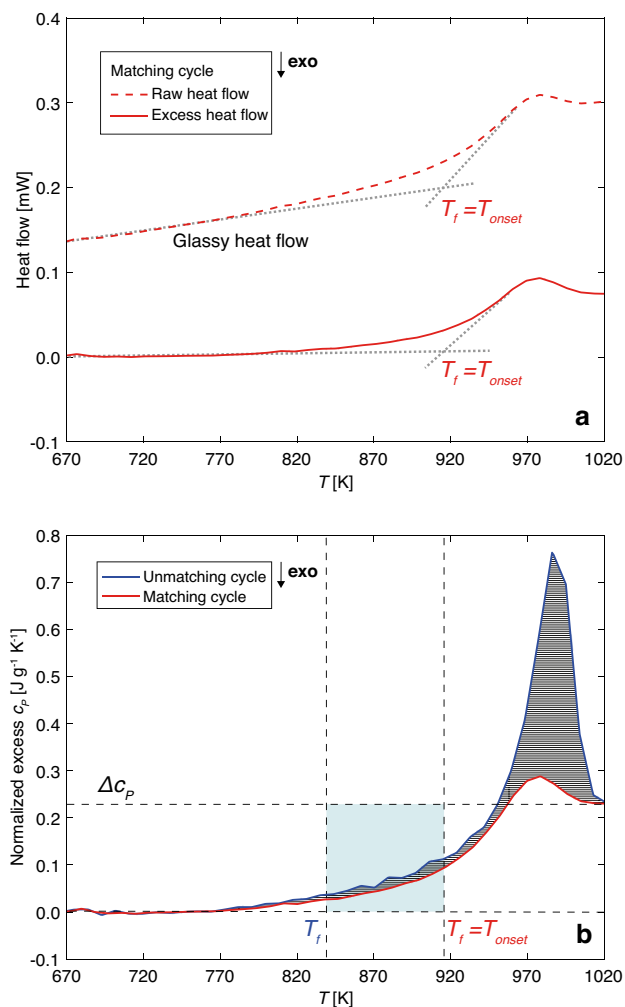
Fig. 5 T_f determination for the DGG-1 using F-DSC. **a** T_f estimation for the matching cycle. Raw heat flow at $q_{c,h} = 1 \times 10^3$ K s^{-1} (dashed line) and calculation of excess heat flow (continuous line). **b** Application of Eq. 7 to determine T_f for the unmatching cycle (blue line, $q_c = 3$ K s^{-1}; $q_h = 1000$ K s^{-1}). The T_f of the matching cycle corresponds to T_{onset} (see text for details)

(from ∼ 0.08 K s^{-1} up to 5×10^3 K s^{-1}) using the same samples, C-DSC and F-DSC adopted here. We thus use their results to externally validate our strategy to derive T_f of unmatching cycles.

We first focus on the standard glass DGG-1 whose viscosity and $T_f - q_c$ relationships are well characterized (Meerlender 1974; Al-Mukadam et al. 2020; 2021b). Figure 6a shows the temperature dependence $-log_{10}(q_c)$ vs. $1/T_f$ provided by Al-Mukadam et al. (2020, 2021b). They found that the $-log_{10}(q_c)$ vs. $1/T_f$ relationship is shifted from the VFT viscosity (left axis in Fig. 6a) by a factor of $K = 11.20 \pm 0.10$ (log$_{10}$ Pa K) (see "Non-Arrhenian approximations" for discussion). As expected (e.g., Webb 2021), the values of T_{onset} of our unmatching cycles (Table 2;

triangles in Fig. 6a) strongly deviate from the main trend, which is crossed only when the matching cycle is considered (i.e., 0.17 K s^{-1} for C-DSC and 1000 K s^{-1} for F-DSC). Here $T_{onset} \equiv T_f$ as discussed above (see "Treatment of DSC measurements and T_f determination").

After the normalization procedure and the application of the area-matching method, the derived T_f from unmatching cycles (Table 2; circles in Fig. 6a) are in basic agreement with the literature data (red line in Fig. 6a) when $q_c < 1000$ K s^{-1}. Only a small deviation of up to –0.2 log units is evident in case of F-DSC. Conversely, when $q_c > 1000$ K s^{-1} is considered (Fig. 6a), our results are systematically lower than the literature data. We speculate that the absence of the exothermic enthalpy relaxation event before the glass transition region (Fig. 4a, c, e), typical of hyper-quenched glasses (i.e., $q_c \gg q_h$; Yue et al. 2002; Dingwell et al. 2004), affects the area calculation of Eq. 7 that in turn leads to an underestimation of T_f values. It thus appears that the F-DSC normalization procedure employed here (i.e., heating rate of 1000 K s^{-1}) does not allow the accurate estimation of exothermic enthalpy relaxation before the glass transition interval for $q_c > 1000$ K s^{-1}. Therefore, T_f values when $q_c > 1000$ K s^{-1} were discarded and not used for the T_f–q_c modeling. Overall, our results demonstrate that the "unified area-matching" strategy holds for determining T_f when q_c ranges between 0.08 and 1000 K s^{-1} using unmatching cycles. We thus conclude that this methodology can be employed also at fast cooling rates typical of F-DSC.

Table 2 lists the estimated T_f from DSC measurements for all samples considered here. As expected (Moynihan et al. 1976), T_f increases with increasing cooling rate. The N-PK52A sample exhibit the lowest T_f that ranges from 746.9 K (0.08 K s^{-1}, C-DSC) to 804.5 K (20,000 K s^{-1}, F-DSC). Di sample exhibits the highest T_f that ranges from 992.5 K (0.08 K s^{-1}, C-DSC) to 1082.0 K (30,000 K s^{-1}, F-DSC). The T_f of DGG-1 melt lies in between N-PK52A and Di samples and varies between 811.8 K (0.08 K s^{-1}, C-DSC) and 936.7 K (30,000 K s^{-1}, F-DSC).

Figure 6b shows the comparison between our T_f and T_{onset} from Al-Mukadam et al. (2020) for the three samples (see Table 2 for details). The figure illustrates an excellent agreement between the two datasets derived by C-DSC measurements, where the RMSE (Root Mean Square Error) estimated is equal to 3.0 K. Conversely, T_f here derived by F-DSC agrees with T_{onset} from Al-Mukadam et al. (2020) when $q_c \leq 1000$ K s^{-1} (RMSE = 11.4 K). For $q_c > 1000$ K s^{-1}, T_f data from N-PK52A and Di glasses show a smaller departure from the 1:1 line with respect to DGG-1 data. However, in analogy to what observed for DGG-1, we decided to conservatively discard these data from further analysis.
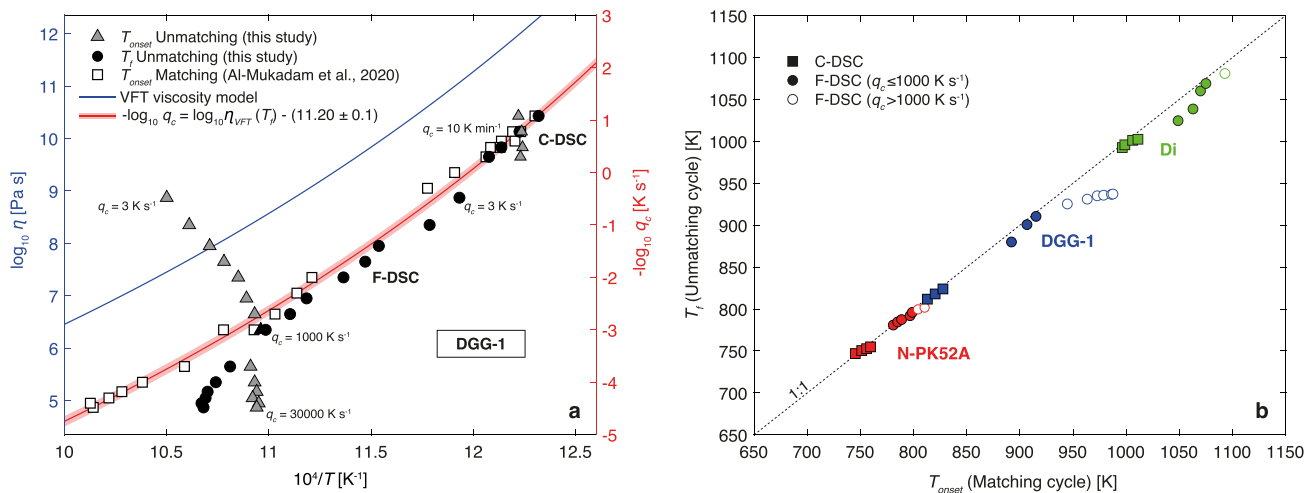
Fig. 6 Validation of strategy to calculate T_f from unmatching cycles. **a** DGG-1 sample. Left axis: Arrhenius plot of viscosity (blue line) using the VFT description (Eq. 6). Right axis: Arrhenius plot of the reciprocal cooling rate. Onsets of the calorimetric glass transition (T_{onset}; triangles) and characteristic fictive temperatures (T_f; circles) obtained by DSC unmatching cycles. The onsets of the calorimetric glass transition (T_{onset}; squares) from Al-Mukadam et al. (2020, 2021b) were evaluated from matching cycles and the model

proposed by the authors relating viscosity and cooling rate (Eq. 8, with a shift factor of $K = 11.20 \pm 0.10$ log_{10} Pa K) are reported for reference. **b** Comparison between T_f from this study and T_{onset} from matching cycles by Al-Mukadam et al. (2020) for the three studied glasses (DGG-1, Di, N-PK52A). Note that only pairs of T_f and T_{onset} from measurements at the same q_c are plotted. Results agree when $q_c < 1000$ K s^{-1}. Data are reported in Table 2

Discussion

Figure 7 shows the Arrhenian plot of $-log_{10}(q_c)$ vs. $10^4/T_f$ of our samples derived using both the unmatching approach employed in this study and the matching approach of Al-Mukadam et al. (2020). We initially fit only C-DSC data using the Arrhenian approximation of Eq. 2 (*Arr. C-DSC Model*). By doing this, we simulate the situation where F-DSC data (high q_c) are unavailable (e.g., Hui et al. 2018). Afterwards, we use Eq. 2 to fit both C-DSC and F-DSC data (*Arr. C-DSC + F-DSC Model*). Finally, we consider three non-Arrhenian models (*non-Arr η Model*, *non-Arr C-DSC Model* and *non-Arr C-DSC + F-DSC Model*), based on the analogy between the temperature-dependence of cooling rate and viscosity (e.g., Scherer 1984; Yue et al. 2004; Al-Mukadam et al. 2020; Stabile et al. 2021). The *non-Arr η Model* requires a priori knowledge of the viscosity–temperature relation, whereas, in *non-Arr C-DSC* and *non-Arr C-DSC + F-DSC Models*, this relationship is internally calibrated based on DSC measurements.

Arrhenian approximations (Arr. C-DSC and Arr. C-DSC + F-DSC models)

When only C-DSC data are considered (*Arr. C-DSC Model*), we obtain activation energy (E_a^q) of 619 kJ mol^{-1} for DGG-1, 1085 kJ mol^{-1} for N-PK52A, and 1407 kJ mol^{-1} for Di (Supplementary Table 1). While this model can obviously reproduce C-DSC data (Fig. 7a), it cannot accurately

reproduce F-DSC data. The estimated RMSE is 0.17 log_{10} K s^{-1} for DGG-1, 0.53 log_{10} K s^{-1} for N-PK52A, and 0.43 log_{10} K s^{-1} for Di. The difference (Δ_q) between measured (q_c) and calculated (q_{cm}) cooling rates depends on the melt fragility (Fig. 7b; Table 3). For instance, when the experimental q_c was 1000 K s^{-1} we obtain $q_{cm} = 1727$ K s^{-1} (3.24 log_{10} K s^{-1};) for DGG-1 sample, $q_{cm} = 17,019$ K s^{-1} (4.23 log_{10} K s^{-1}) for Di and $q_{cm} = 3832$ K s^{-1} (3.58 log_{10} K s^{-1}) for N-PK52A.

When C-DSC and F-DSC are considered (*Arr. C-DSC + F-DSC Model*), lower activation energies are obtained (581 kJ mol^{-1} for DGG-1, 923 kJ mol^{-1} for N-PK52A and 1121 kJ mol^{-1} for Di; Supplementary Table 1). This results in a more accurate estimation of q_{cm} and thereby lower RSME (Fig. 7b inset; RMSE$_{DGG-1} = 0.14$ log_{10} K s^{-1}; RMSE$_{N-PK52A} = 0.08$ log_{10} K s^{-1}; RMSE$_{Di} = 0.24$ log_{10} K s^{-1}). Here, cooling rates of $q_{cm} = 1278$ K s^{-1} (3.11 log_{10} K s^{-1}) for DGG-1, 2281 K s^{-1} (3.36 log_{10} K s^{-1}) for Di, and 839 K s^{-1} (2.92 log_{10} K s^{-1}) for N-PK52A are derived when the experimental q_c is 1000 K s^{-1} (Table 3).

Figure 7 also shows T_{onset} from Al-Mukadam et al. (2020) for comparison. Except for N-PK52A sample, both Arrhenian models fail to reproduce this dataset when $q_c > 1000$ K s^{-1} (Fig. 7a).

Non-Arrhenian approximations

Here we use the analogy between the $-log_{10}(q_c)$ vs. $1/T_f$ and the $log_{10}(\eta)$ vs. $1/T$ to derive q_c when the temperature

Table 2 Onsets of the calorimetric glass transition (T_{onset}) and characteristic fictive temperatures (T_f) of the studied glasses obtained by DSC unmatching cycles

DSC-type	q_c (K s^{-1})	DGG–1			N–PK52A		Di	
		$T_{onset\,(unmatching)}$ (K)	T_f (K)	$^{\#}T_{onset\,(matching)}$ (K)	T_f (K)	$^{\#}T_{onset\,(matching)}$ (K)	T_f (K)	$^{\#}T_{onset\,(matching)}$ (K)
C-DSC	0.08	818.7	811.8	813.0	746.9	745.2	992.5	996.3
	0.17	818.0	818.0	820.3	750.5	751.2	995.8	998.7
	0.33	818.2	824.0	827.6	752.7	755.8	1001.1	1006.0
	0.50	818.3	828.1	–	754.9	759.5	1002.4	1011.0
F-DSC	3	952.3	838.1	–	–	–	–	–
	10	942.5	848.5	–	–	–	–	–
	25	933.6	866.7	–	778.9	–	1024.5	1048.8
	50	927.3	871.8	–	780.9	780.9	1031.6	–
	100	921.4	879.9	892.1	784.6	785.0	1038.5	1062.8
	200	–	–	898.0	787.4	788.7	–	1061.3
	250	918.5	894.1	–	–	–	1048.9	–
	500	914.6	900.6	906.7	792.0	796.7	1060.0	1069.9
	750	–	–	–	–	–	–	1072.8
	1000	912.3	910.4	915.2	796.0	798.7	1068.9	1074.9
	1500	–	–	–	–	–	–	1080.0
	2000	–	–	–	–	–	–	1084.1
	2500	–	–	–	799.6*	804.1	–	–
	5000	916.6*	925.3*	944.6	801.7*	810.4	1080.8*	1092.8
	7500	–	–	–	803.5*	–	–	–
	10,000	914.6*	931.0*	963.3	802.9*	–	1086.4*	–
	15,000	914.2*	935.0*	972.7	804.1*	–	1088.3*	–
	20,000	916.1*	935.7*	978.7	804.5*	–	1086.7*	–
	25,000	913.1*	937.1*	987.5	–	–	1082.5*	–
	30,000	914.0*	936.7*	986.1	–	–	1081.0*	–

Onsets of the calorimetric glass transition (T_{onset}) from DSC matching cycles by Al-Mukadam et al. (2020) are reported for comparison. Stars (*) indicate data excluded from subsequent analyses (see text for details)

dependence of viscosity is known. This analogy builds on the equivalence between the activation energy for viscous flow (E_a^{η}) and the activation energy for structural relaxation E_a^q determined by DSC (Scherer 1984; Moynihan et al. 1996; Al-Mukadam et al. 2020, 2021a, b; Di Genova et al. 2020a). Scherer (1984) first proposed a parallel shift factor correlating viscosity and q_c following the equation:

$$K = log_{10}(|q_c|) + log_{10}\eta(T_f) \qquad (8)$$

where $\eta(T_f)$ is the viscosity at T_f.

In the following, we examine two cases: (i) $log_{10}(\eta)$ at T_f is independently known (*non-Arr. η Model*) and (ii) $log_{10}(\eta)$ at T_f is derived from C-DSC and F-DSC data (*non-Arr. C-DSC Model*, and *non-Arr. C-DSC + F-DSC Model*).

Viscosity is independently known (non-Arr. η Model)

The viscosity–temperature dependence of melts used here is known (Al-Mukadam et al. 2020) over a large interval

($\sim 10^1 < \eta < \sim 10^{12}$ Pa s) and described by the non-Arrhenian VFT equation (Eq. 6; Supplementary Table 2). Therefore, T_f can be used to calculate $\eta(T_f)$ and obtain K (Eq. 8; Supplementary Fig. 1). We use either the C-DSC subset, the F-DSC subset, or the entire dataset (C-DSC + F-DSC). Slightly different K values are obtained for different samples and DSC devices (Supplementary Tables 2 and 3). The lowest mean value (11.11 ± 0.06 log$_{10}$ Pa K) is calculated for Di (only C-DSC data), while the highest (11.49 ± 0.09 log$_{10}$ Pa K) for DGG-1 (only F-DSC). By combining C-DSC and F-DSC data, we obtain $K = 11.40 \pm 0.15$ log$_{10}$ Pa K for DGG, $K = 11.34 \pm 0.11$ log$_{10}$ Pa K for N-PK52A and $K = 11.30 \pm 0.20$ log$_{10}$ Pa K for Di. We thus provide a global value of $K = 11.35 \pm 0.16$ log$_{10}$ Pa K that agrees with previous data within the standard deviation ($11.20 \pm 0.10 < K < 11.35 \pm 0.10$; Scherer 1984; Yue et al. 2004; Chevrel et al. 2013; Shawe and Hess, 2019; Al-Mukadam et al. 2020, 2021b; Di Genova et al. 2020b; Stabile et al. 2021).

The $K_{mean} = 11.35$ log$_{10}$ Pa K allows the estimation of q_c up to 1000 K s^{-1} with a RMSE of 0.15 log$_{10}$
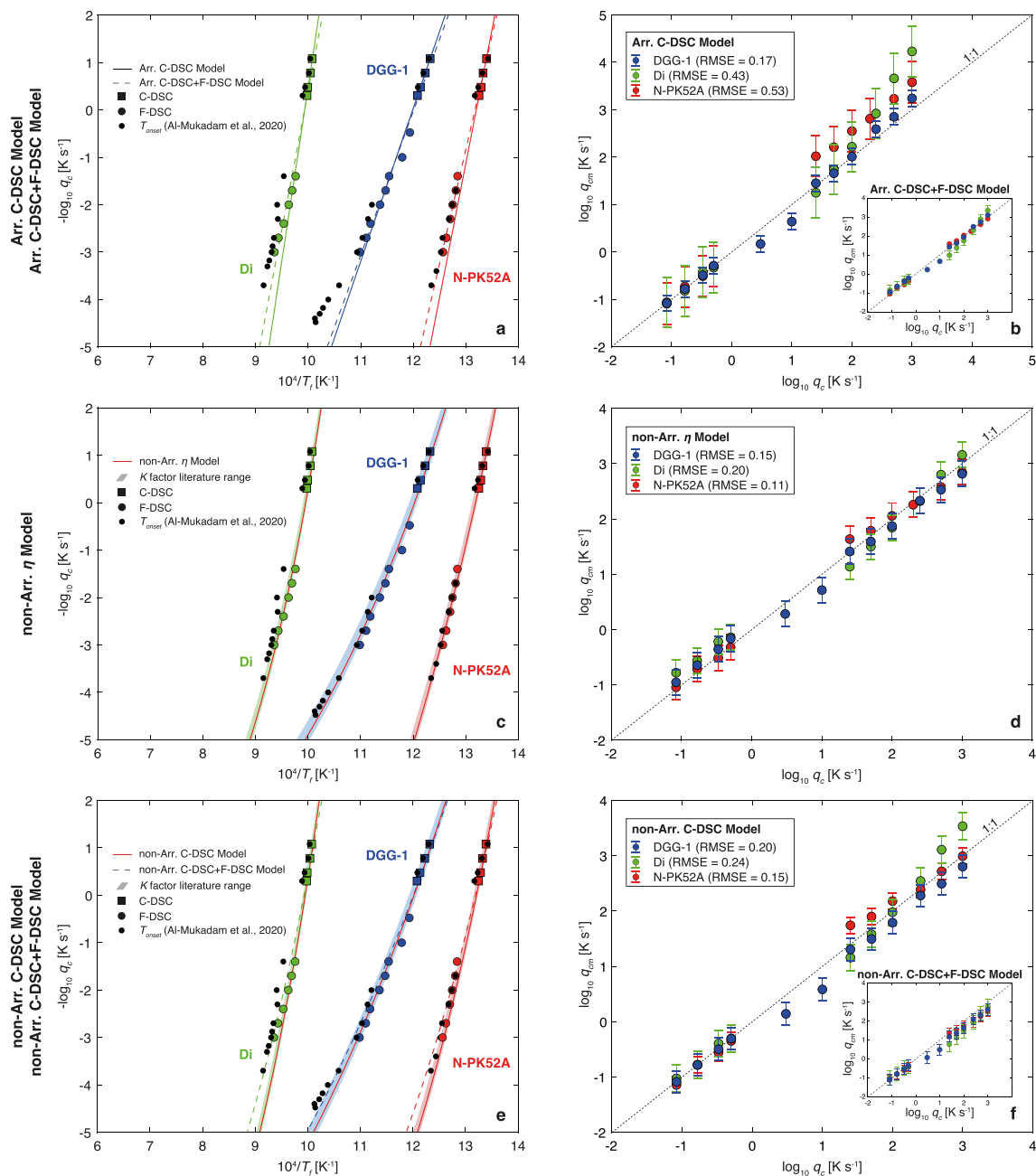
Fig. 7 C-DSC (squares) and F-DSC (circles) data, their modeling (**a**, **c**, **e**). In **a**, **c**, and **e**, data from Al-Mukadam et al. (2020) are reported for comparison purpose (small black circles). **a** Solid and dashed lines represent the Arrhenian models based only on C-DSC data (*Arr. C-DSC Model*) and the combination of C-DSC and F-DSC data (*Arr. C-DSC+F-DSC Model*), respectively. **c**, **e** Non-Arrhenian fitting of data according to Eq. 8, using **c** the VFT equation (Eq. 6) (*non-Arr. η Model*) and **e** internally calibrated (C-DSC-based and C-DSC+F-DSC-based) MYEGA equation (Eq. 10) (*non-Arr. C-DSC*

Model, solid lines; *non-Arr. C-DSC+F-DSC Model*, dashed lines). Red lines correspond to Eq. 8 (where $K_{mean} = 11.35$ $\log_{10}$ Pa K as derived in this study). Shaded areas correspond to the K_{mean} uncertainty (± 0.16 $\log_{10}$ Pa K). **b**, **d**, **f** Experimentally imposed (q_c) vs. modelled (q_{cm}) cooling rates for the different models: **b** *Arr. C-DSC Model* (*Arr. C-DSC+F-DSC Model* is reported in the inset); **d** *non-Arr. η Model*; **e** *non-Arr. C-DSC Model* (*non-Arr. C-DSC+F-DSC Model* is reported in the inset). Dotted lines represent the 1:1 line; all calculated data are reported with relative standard deviations

Table 3 Cooling rates estimated (q_{cm}) according to the different model proposed in this study

Sample	DSC-type	$log_{10} q_c$ (K s⁻¹)	Arr. C-DSC Model $log_{10} q_{cm}$ (K s⁻¹)	Arr. C-DSC+F-DSC Model $log_{10} q_{cm}$ (K s⁻¹)	non-Arr. η Model $log_{10} q_{cm}$ (K s⁻¹)	non-Arr. C-DSC Model $log_{10} q_{cm}$ (K s⁻¹)	non-Arr. C-DSC+F-DSC Model $log_{10} q_{cm}$ (K s⁻¹)
DGG-1	C-DSC	− 1.08	− 1.08	− 0.95	− 0.95	− 1.09	− 1.07
		− 0.78	**− 0.78**	**− 0.66**	**− 0.64**	**− 0.78**	**− 0.78**
		− 0.48	− 0.49	− 0.39	− 0.35	− 0.50	− 0.51
		− 0.30	− 0.29	− 0.21	− 0.16	− 0.31	− 0.33
	F-DSC	0.48	0.17	0.23	0.28	0.14	0.09
		1.00	0.64	0.67	0.72	0.58	0.51
		1.40	1.45	1.43	1.41	1.31	1.19
		1.70	1.66	1.63	1.59	1.50	1.37
		2.00	2.01	1.95	1.87	1.79	1.65
		2.40	2.59	2.50	2.33	2.28	2.12
		2.70	2.85	2.74	2.53	2.49	2.32
		3.00	**3.24**	**3.11**	**2.82**	**2.80**	**2.62**
			RMSE = 0.17	RMSE = 0.14	RMSE = 0.15	RMSE = 0.20	RMSE = 0.29
N-PK52A	C-DSC	− 1.08	− 1.09	− 1.05	− 1.04	− 1.14	− 1.09
		− 0.78	**− 0.73**	**− 0.75**	**− 0.71**	**− 0.78**	**− 0.78**
		− 0.48	− 0.51	− 0.56	− 0.51	− 0.56	− 0.59
		− 0.30	− 0.30	− 0.38	− 0.32	− 0.35	− 0.41
	F-DSC	1.40	2.02	1.59	1.64	1.74	1.39
		1.70	2.21	1.75	1.79	1.90	1.53
		2.00	2.55	2.04	2.06	2.18	1.78
		2.30	2.81	2.26	2.26	2.39	1.96
		2.70	3.23	2.62	2.58	2.72	2.25
		3.00	**3.58**	**2.92**	**2.85**	**2.99**	**2.50**
			RMSE = 0.43	RMSE = 0.08	RMSE = 0.11	RMSE = 0.15	RMSE = 0.26
Di	C-DSC	− 1.08	− 1.06	− 0.85	− 0.78	− 1.02	− 0.97
		− 0.78	**− 0.82**	**− 0.66**	**− 0.56**	**− 0.78**	**− 0.78**
		− 0.48	− 0.42	− 0.35	− 0.22	− 0.39	− 0.47
		− 0.30	− 0.33	− 0.28	− 0.14	− 0.30	− 0.40
	F-DSC	1.40	1.25	0.99	1.14	1.16	0.79
		1.70	1.74	1.38	1.50	1.58	1.13
		2.00	2.22	1.76	1.84	1.98	1.47
		2.40	2.92	2.31	2.32	2.54	1.94
		2.70	3.66	2.90	2.80	3.11	2.41
		3.00	**4.23**	**3.36**	**3.16**	**3.53**	**2.78**
			RMSE = 0.53	RMSE = 0.24	RMSE = 0.20	RMSE = 0.24	RMSE = 0.37

Bold numbers highlight matching cycle measurements

K s⁻¹ for DGG-1, 0.20 log_{10} K s⁻¹ for Di, and 0.11 log_{10} K s⁻¹ for N-PK52A. For instance, the *non-Arr. η Model* returns $q_{cm} = 655$ K s⁻¹ (2.82 log_{10} K s⁻¹) for DGG-1, $q_{cm} = 1443$ K s⁻¹ (3.16 log_{10} K s⁻¹) for Di, and $q_{cm} = 705$ K s⁻¹ (2.85 log_{10} K s⁻¹) for N-PK52A, when the experimental q_c is 1000 K s⁻¹ (Table 3; Fig. 7d).

Notably, the *non-Arr η Model* excellently fits the T_{onset} from Al-Mukadam et al. (2020) up to 30,000 K s⁻¹ within the error (Fig. 7c).

Viscosity is internally calibrated by DSC measurements (non-Arr. C-DSC and non-Arr. C-DSC + F-DSC models)

Natural and synthetic melts (including those of volcanological interest) can undergo crystallization or exsolution of volatiles on the timescale of viscosity measurements near T_g (Liebske et al. 2003; Di Genova et al. 2017, 2020a, b). Because crystallization and dehydration around T_g lead to the absence of pure melt viscosity data near T_g (Dingwell

et al. 2004; Chevrel et al. 2013), the use of DSC offers a viable route to derive melt viscosity due to its lower impact on melt chemistry and texture (Dingwell et al. 2004; Chevrel et al. 2013; Di Genova et al. 2020b; Langhammer et al. 2021; Stabile et al. 2021).

Here we use the viscosity–temperature description provided by the Mauro-Yue-Ellison-Gupta-Allan equation (MYEGA; Mauro et al. 2009):

$$log_{10}\eta = log_{10}\eta_\infty + \left(12 - log_{10}\eta_\infty\right)\frac{T_g}{T}\exp\left[\left(\frac{m_{vis}}{12 - log_{10}\eta_\infty} - 1\right)\left(\frac{T_g}{T} - 1\right)\right] \tag{9}$$

where $log_{10}(\eta_\infty)$ is the limit of viscosity logarithm at infinite T (-2.93 log_{10} Pa s, Zheng et al., 2011), T_g is the glass transition temperature derived by DSC via a matching measurement at 10 K min^{-1} ($T_g \equiv T_{onset}$), and m_{vis} is the liquid fragility index (Eq. 4). Because η and q_c are related to each other via Eq. 8 and $K_{mean} = 11.35$ log_{10} Pa K, from Eq. 9 we can derive:

$$-log_{10}q_c = -14.28 + 14.93\frac{T_g}{T_f}\exp\left[\left(\frac{m_{DSC}}{14.93} - 1\right)\left(\frac{T_g}{T_f} - 1\right)\right] \tag{10}$$

where m_{DSC} is the calorimetric fragility (Zheng et al. 2017) according to Eq. 5. m_{vis} linearly correlates ($\sim$1:1) with m_{DSC} (derived by C-DSC) over a wide range of kinetic fragility (e.g., Chen et al. 2014; Zheng et al. 2017; Al-Mukadam et al. 2021b).

We consider two cases based on C-DSC data (*non-Arr. C-DSC Model*) and C-DSC + F-DSC data (*non-Arr. C-DSC + F-DSC Model*).

For *non-Arr. C-DSC model*, we use E_a^q (Supplementary Table 1) derived from the *Arr. C-DSC Model* and Eq. 5 and find $m_{DSC} = 39.5$ for DGG-1, $m_{DSC} = 75.5$ for N-PK52A and $m_{DSC} = 73.8$ for Di. These values well match the m_{vis} provided by Al-Mukadam et al. (2020) (cf. Figure 2).

We estimate (Eq. 10) q_c up to 1000 K s^{-1} with a RMSE of 0.20 log_{10} K s^{-1} for DGG-1, 0.24 log_{10} K s^{-1} for Di, and 0.15 log_{10} K s^{-1} for N-PK52A (Table 3; Fig. 7f). The *non-Arr. C-DSC Model* predicts $q_{cm} = 637$ K s^{-1} (2.80 log_{10} K s^{-1}) for DGG-1, $q_{cm} = 3418$ K s^{-1} (3.53 log_{10} K s^{-1}) for Di, and $q_{cm} = 981$ K s^{-1} (2.99 log_{10} K s^{-1}) for N-PK52A, when the experimental q_c is 1000 K s^{-1} (Table 3; Fig. 7f).

The *non-Arr. C-DSC + F-DSC Model* finds slightly lower fragility values. For instance, $m_{DSC} = 37.1$ for DGG-1, $m_{DSC} = 64.2$ for N-PK52A and $m_{DSC} = 58.8$ for Di, according to a lower E_a^q (Supplementary Table 1) derived from the *Arr. C-DSC + F-DSC Model* and Eq. 5. Here, cooling rates of $q_{cm} = 414$ K s^{-1} (2.62 log_{10} K s^{-1}) for DGG-1, 598 K s^{-1} (2.78 log_{10} K s^{-1}) for Di, and 314 K s^{-1} (2.50 log_{10} K s^{-1}) for N-PK52A are derived (Table 3) when the experimental q_c is 1000 K s^{-1}. The model underestimates F-DSC cooling rates,

leading to a general RMSE of 0. 29 log_{10} K s^{-1} for DGG-1, 0.37 log_{10} K s^{-1} for Di, and 0.26 log_{10} K s^{-1} for N-PK52A.

Finally, Fig. 7e shows that the *non-Arr. C-DSC + F-DSC Model* better captures the T_{onset} related to the ultra-fast cooling rates from Al-Mukadam et al. (2020) due to the increased number of data considered. This reflects on a better constrain to the ultra-fast cooling region.

## Comparison between models within and outside the calibration range

The proposed models return q_c of our melts to different extents (Fig. 7). In general, with the exception of the *Arr. C-DSC Model*, all the models can predict the experimentally imposed cooling rate with a good degree of approximation.

The *Arr. C-DSC Model*, based only on C-DSC, fails to predict F-DSC data due to the narrow range of q_c employed by C-DSC ($\sim$0.08 $\leq q_c \leq$ 0.5 K s^{-1}). This results in the unreliable extrapolation of q_c to higher values (RMSE = 0.37 log_{10} K s^{-1}). Conversely, the *Arr. C-DSC + F-DSC Model*, based on C-DSC and F-DSC, allows the estimation of q_c up to 1000 K s^{-1} with an RMSE = 0.16 log_{10} K s^{-1}). The *Arr. C-DSC + F-DSC Model* well predicts q_{cm} in a $\eta(T_f)$ range varying between $\sim$10^8 and $\sim$10^{12} Pa s (Supplementary Fig. 1 and Supplementary Table 1). This viscosity interval is analogous to that commonly investigated through micropenetration viscometry, where silicate melts approximate Arrhenian fluids (e.g., Hess et al. 1995).

All non-Arrhenian models proved to successfully predict q_c in the investigated cooling rates interval. This can be achieved using the chemically independent shift factor ($K = 11.35 \pm 0.16$ log_{10} Pa K, Eq. 8). If the viscosity-temperature relationship is known, the *non-Arr. η Model* represents the most robust procedure for obtaining q_c values (Table 3, RMSE of 0.15 log_{10} K s^{-1}) also capturing the T_{onset} related to ultra-fast q_c from Al-Mukadam et al. (2020). Alternatively, the *non-Arr. C-DSC* and *non-Arr. C-DSC + F-DSC Models* (mean RMSE of 0.20 log_{10} K s^{-1} and 0.31 log_{10} K s^{-1}, respectively) offer a viable route when viscosity data are unavailable.

Figure 8 depicts the models' performances in the entire cooling range typical of volcanic materials. The models substantially diverge, both in the slow-cooling rate ($q_c < 10^{-1}$ K s^{-1}) and fast-cooling rate ($q_c > 10^3$ K s^{-1}) regimes. It is therefore apparent that, when extensive extrapolation is needed (e.g., for the study of fast-quenched submarine materials or slow-quenched lava flows and vitrophyres), the choice of the models becomes non-trivial.

Fig. 8 Extrapolation of the proposed models over the q_c range of natural volcanic glasses (see Fig. 1)
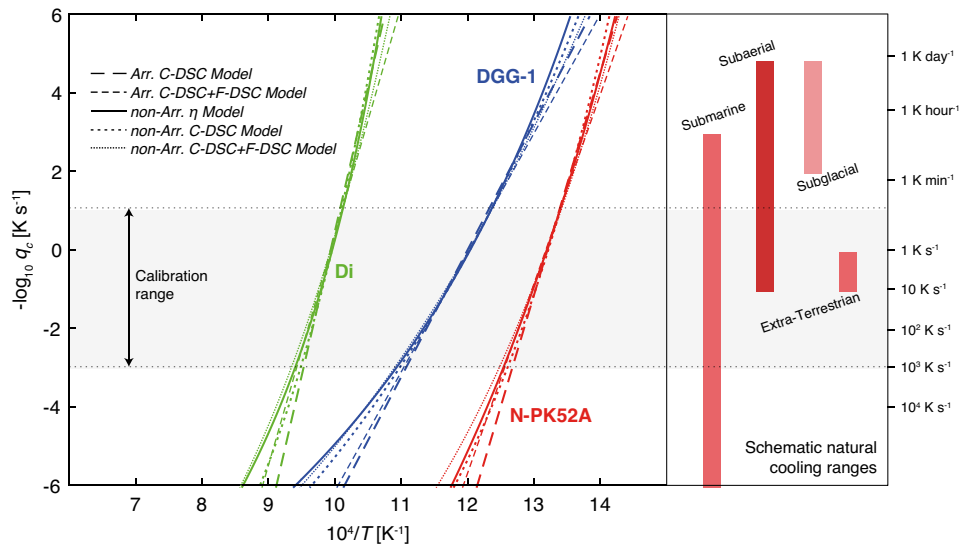

The analogy between E_a^q and E_a^η (Scherer 1984; Moynihan et al. 1996; Al-Mukadam et al. 2020, 2021a, b; Di Genova et al. 2020a, b) makes it plausible to hypothesize the T_f–q_c relationship as non-Arrhenian in the entire cooling range typical of volcanic environments (Fig. 8; 10^{-5} K s^{-1} $\leq q_c \leq 10^6$ K s^{-1}), as for viscosity in the whole temperature range. As a consequence, in the case of ultra-fast and ultra-slow cooling rates, the employment of a non-Arrhenian model is expected to provide more reliable data and should be preferred. In contrast, the constant E_a^q of Arrhenian models is expected to produce an overestimation of q_c for fast- and slow-quenched glasses (Fig. 8).

Geospeedometry recipes: a "how-to" protocol for cooling rate determination

Figure 9 summarizes a practical "how-to" guide to determine the cooling rate of glasses, depending on the available dataset.

The choice of the appropriate calorimeter should be dictated in the first place by the expected range of cooling rates, based on the geological setting of the studied glass (Fig. 1). In addition, F-DSC is more suited when small amounts of glass material are available for the analysis and when the sample is prone to rapid modifications at high temperatures.

Fig. 9 Schematic flowchart for the determination of the unknown cooling rate embedded in glasses
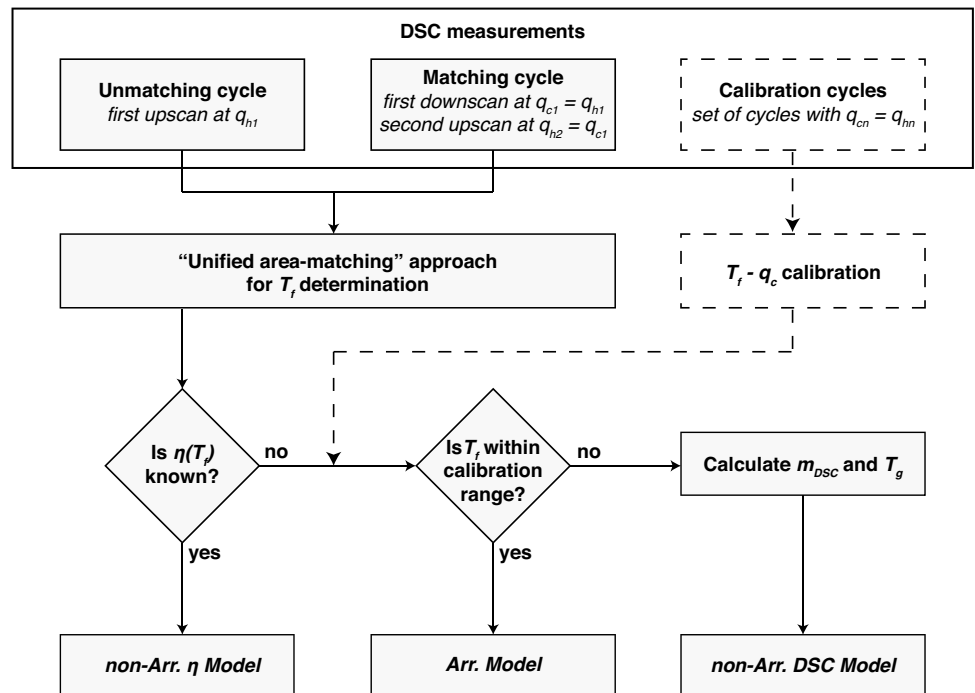
The "unified area-matching" holds for glasses subjected to q_c between ~0.08 and ~0.5 K s^{-1} in the C-DSC and between 3 and 1000 K s^{-1} in the F-DSC. The method requires two DSC upscans (unmatching and matching cycles) to estimate T_f of the glass with unknown thermal history (Eq. 7).

A separate set of matching cycles ($q_{c2,h2}$, $q_{c3,h3}$, $q_{cn,hn}$, ...) is required for the calibration of the T_f–q_c relationship. Arrhenian models (Eq. 2) should be only used when T_f of the glass with unknown cooling history falls within or close to the DSC (C-DSC or F-DSC) calibration range. For C-DSC measurements this conditions corresponds to T_f close to T_g (as defined in Eq. 1).

When a significant extrapolation is required, a non-Arrhenian model represents the best protocol to estimate q_c. Notably, the *non-Arr η Model* does not require the calibration of the T_f–q_c relationship through matching cycles. This approach only requires two DSC measurements (i.e., the first upscan on the glass with an unknown cooling history and the rejuvenated glass matching cycle). Once T_f is determined, the application of Eq. 8 allows the estimation of the unknown q_c, provided the viscosity of the sample is independently known.

However, crystallization and dehydration of melts may hamper the viscosity measurements (Richet et al. 1996; Liebske et al. 2003; Zheng et al. 2017, 2019; Di Genova et al. 2020a, b) and pure melt viscosity data near T_g may be lacking. Here, the non-Arrhenian DSC-based models offer an alternative procedure for q_c determination. The application of these models requires a C-DSC matching cycle at $q_{c,h} = 10$ K min^{-1} to constrain T_g (Eq. 1; $Tg \equiv T_{onset}$) and a set of matching cycles at variable $q_{c,h}$ (C-DSC and/or F-DSC) to constrain the calorimetric fragility (m_{DSC}; Eq. 5). Once these parameters are determined, the unknown q_c is computed via Eq. 10. It should be noted that these models are not constrained by data in the low-viscosity/high-cooling rates regime (a constant value of $log_{10}(\eta_\infty) = -2.93$ is used in Eq. 9 and 10). Consequently, when extrapolation is needed, they are expected to perform better in the slow cooling rate regime and may progressively becomes less accurate at fast cooling rates. In addition, since the determination of m_{DSC} is slightly affected by the matching calibration interval over which is averaged, the use of C-DSC should be preferred for extrapolation towards slow cooling rates, whereas the use of a F-DSC is expected to reduce the extrapolation uncertainty at very fast cooling rates (i.e., $q_c > 10^3$ K s^{-1}).

Concluding remarks

This study combined conventional and flash calorimetry to estimate the cooling rate (q_c) of glass-forming melts over four orders of magnitude, from 0.08 K s^{-1} (5 K min^{-1}) to 1000 K s^{-1}. Our study is based on the relationship between q_c and the glass's limiting fictive temperature (T_f).

We demonstrate that the "unified area-matching" approach for calculating T_f proposed by Guo et al. (2011) holds for q_c up to 1000 K s^{-1}. This is central for obtaining the T_f of the glass quenched at an unknown cooling rate without the need to perform empirical fitting of heat capacity measurements.

We show that the Arrhenian extrapolation of $-log_{10}(q_c)$ over $1/T_f$ can overestimate the unknown q_c. The non-Arrhenian description of $-log_{10}(q_c)$ over $1/T_f$ offers the most accurate estimation of q_c, especially when q_c falls outside the calibration range. The non-Arrhenian description requires, however, the knowledge of the melt viscosity. Because volcanic melt can be prone to crystallization and dehydration during viscosity measurements, we present an alternative route to derive q_c without performing viscosity measurements.

References

Al-Mukadam R, Di Genova D, Bornhöft H, Deubener J (2020) High rate calorimetry derived viscosity of oxide melts prone to crystallization. J Non Cryst Solids 536:119992. https://doi.org/10.1016/j.jnoncrysol.2020.119992

Al-Mukadam R, Zandona A, Deubener J (2021a) Kinetic fragility of pure TeO2 glass. J Non Cryst Solids 554:120595. https://doi.org/10.1016/j.jnoncrysol.2020.120595

Al-Mukadam R, Götz IK, Stolpe M, Deubener J (2021b) Viscosity of metallic glass-forming liquids based on Zr by fast-scanning calorimetry. Acta Mater 221:117370. https://doi.org/10.1016/j.actamat.2021.117370

Angell CA (1985) Spectroscopy simulation and scattering, and the medium range order problem in glass. J Non Cryst Solids 73:1–17

Archer DG (1993) Thermodynamic properties of synthetic sapphire (α-Al$_2$O$_3$), standard reference material 720 and the effect of

temperature-scale differences on thermodynamic properties. J Phys Chem Ref Data 22:1441–1453. https://doi.org/10.1063/1.555931

Bauer U, Behrens H, Fechtelkord M et al (2015) Water- and boron speciation in hydrous soda-lime-borate glasses. J Non Cryst Solids 423–424:58–67. https://doi.org/10.1016/j.jnoncrysol.2015.05.004

Behrens H (2020) Water speciation in oxide glasses and melts. Chem Geol 558:119850. https://doi.org/10.1016/j.chemgeo.2020.119850

Behrens H, Nowak M (2003) Quantification of H_2O speciation in silicate glasses and melts by IR spectroscopy—in situ versus quench techniques. Phase Transitions 76:45–61. https://doi.org/10.1080/0141159031000076048

Benne D, Behrens H (2003) Water solubility in haplobasaltic melts. Eur J Mineral 15:803–814. https://doi.org/10.1127/0935-1221/2003/0015-0803

Cashman KV (2020) Crystal size distribution (CSD) analysis of volcanic samples: advances and challenges. Front Earth Sci 8:1–17. https://doi.org/10.3389/feart.2020.00291

Chen Z, Li Z, Zhang Y et al (2014) Calorimetric determination of fragility in glass forming liquids: Tf vs Tg-onset methods. Eur Phys J E 37:1–7. https://doi.org/10.1140/epje/i2014-14052-y

Chevrel MO, Giordano D, Potuzak M et al (2013) Physical properties of $CaAl_2Si_2O_8$-$CaMgSi_2O_6$-FeO-Fe_2O_3 melts: analogues for extra-terrestrial basalt. Chem Geol 346:93–105. https://doi.org/10.1016/j.chemgeo.2012.09.004

DeBolt MA, Easteal AJ, Macedo PB, Moynihan CT (1976) Analysis of structural relaxation in glass using rate heating data. J Am Ceram Soc 59:16–21

Di Fiore F, Vona A, Kolzenburg S et al (2021) An extended rheological map of pāhoehoe—'A'ā transition. J Geophys Res Solid Earth 126:1–23. https://doi.org/10.1029/2021JB022035

Di Genova D, Romano C, Hess KU et al (2013) The rheology of peralkaline rhyolites from Pantelleria Island. J Volcanol Geotherm Res 249:201–216. https://doi.org/10.1016/j.jvolgeores.2012.10.017

Di Genova D, Kolzenburg S, Wiesmaier S et al (2017) A compositional tipping point governing the mobilization and eruption style of rhyolitic magma. Nature 552:235–238. https://doi.org/10.1038/nature24488

Di Genova D, Zandona A, Deubener J (2020a) Unravelling the effect of nano-heterogeneity on the viscosity of silicate melts: implications for glass manufacturing and volcanic eruptions. J Non Cryst Solids 545:120248. https://doi.org/10.1016/j.jnoncrysol.2020.120248

Di Genova D, Brooker RA, Mader HM et al (2020b) In situ observation of nanolite growth in volcanic melt: a driving force for explosive eruptions. Sci Adv. https://doi.org/10.1126/sciadv.abb0413

Dingwell DB, Courtial P, Giordano D, Nichols ARL (2004) Viscosity of peridotite liquid. Earth Planet Sci Lett 226:127–138. https://doi.org/10.1016/j.epsl.2004.07.017

Fanara S, Behrens H (2011) Proton conduction in hydrous glasses of the join CaAl2Si2O8–CaMgSi2O6: an impedance and infrared spectroscopic study. J Chem Phys 134:194505. https://doi.org/10.1063/1.3589898

Fulcher GS (1925) Analysis of recent measurements of the viscosity of glasses. J Am Ceram Soc 8:339–355. https://doi.org/10.1111/j.1151-2916.1925.tb16731.x

Giordano D, Russell JK, Dingwell DB (2008) Viscosity of magmatic liquids: a model. Earth Planet Sci Lett 271:123–134. https://doi.org/10.1016/j.epsl.2008.03.038

Giuliani L, Iezzi G, Hippeli T et al (2020) The onset and solidification path of a basaltic melt by in situ differential scanning calorimetry (DSC) and ex situ investigations. Front Earth Sci 8:1–15. https://doi.org/10.3389/feart.2020.00337

Gonnermann HM, Manga M (2012) Dynamics of magma ascent in the volcanic conduit. Model Volcan Process Phys Math Volcanism. https://doi.org/10.1017/CBO9781139021562.004

Gottsmann J, Dingwell DB (2001a) Cooling dynamics of spatter-fed phonolite obsidian flows on Tenerife, Canary Islands. J Volcanol Geotherm Res 105:323–342. https://doi.org/10.1016/S0377-0273(00)00262-6

Gottsmann J, Dingwell DB (2001b) The cooling of frontal flow ramps: a calorimetric study on the Rocche Rosse rhyolite flow, Lipari, Aeolian Islands, Italy. Terra Nova 13:157–164. https://doi.org/10.1046/j.1365-3121.2001.00332.x

Gottsmann J, Dingwell DB (2002) The thermal history of a spatter-fed lava flow: the 8-ka pantellerite flow of Mayor Island, New Zealand. Bull Volcanol 64:410–422. https://doi.org/10.1007/s00445-002-0220-7

Gottsmann J, Harris AJL, Dingwell DB (2004) Thermal history of Hawaiian pāhoehoe lava crusts at the glass transition: implications for flow rheology and emplacement. Earth Planet Sci Lett 228:343–353. https://doi.org/10.1016/j.epsl.2004.09.038

Guo X, Potuzak M, Mauro JC et al (2011) Unified approach for determining the enthalpic fictive temperature of glasses with arbitrary thermal history. J Non Cryst Solids 357:3230–3236. https://doi.org/10.1016/j.jnoncrysol.2011.05.014

Helo C, Clague DA, Dingwell DB, Stix J (2013) High and highly variable cooling rates during pyroclastic eruptions on Axial Seamount, Juan de Fuca Ridge. J Volcanol Geotherm Res 253:54–64. https://doi.org/10.1016/j.jvolgeores.2012.12.004

Hess K-U, Dingwell DB, Webb SL (1995) The influence of excess alkalis on the viscosity of a haplogranitic melt. Am Mineral 80:297–304

Hui H, Zhang Y (2007) Toward a general viscosity equation for natural anhydrous and hydrous silicate melts. Geochim Cosmochim Acta 71:403–416

Hui H, Hess KU, Zhang Y et al (2018) Cooling rates of lunar orange glass beads. Earth Planet Sci Lett 503:88–94. https://doi.org/10.1016/j.epsl.2018.09.019

Iezzi G, Elbrecht AL, Davis M et al (2017) Glass stability (GS) of chemically complex (natural) sub-alkaline glasses. J Non Cryst Solids 477:21–30. https://doi.org/10.1016/j.jnoncrysol.2017.09.047

Kenderes SM, Whittington AG (2021) Faster geospeedometry: a Monte Carlo approach to relaxational geospeedometry for determining cooling rates of volcanic glasses. Chem Geol 581:120385. https://doi.org/10.1016/j.chemgeo.2021.120385

Knoche R, Dingwell DB, Seifert FA, Webb SL (1994) Non-linear properties of supercooled liquids in the system Na_2O-SiO_2. Chem Geol 116:1–16. https://doi.org/10.1016/0009-2541(94)90154-6

Kueppers U, Nichols ARL, Zanon V et al (2012) Lava balloons-peculiar products of basaltic submarine eruptions. Bull Volcanol 74:1379–1393. https://doi.org/10.1007/s00445-012-0597-x

Langhammer D, Di Genova D, Steinle-Neumann G (2021) Modeling the viscosity of anhydrous and hydrous volcanic melts. Geochem Geophys Geosyst 22:1–26. https://doi.org/10.1029/2021gc009918

Lavallée Y, Wadsworth FB, Vasseur J et al (2015) Eruption and emplacement timescales of ignimbrite super-eruptions from thermo-kinetics of glass shards. Front Earth Sci 3:1–11. https://doi.org/10.3389/feart.2015.00002

Liebske C, Behrens H, Holtz F, Lange RA (2003) The influence pf pressure and composition on the viscosity of andesitic melts. Geochim Cosmochim Acta 67:473–485. https://doi.org/10.1016/S0016-7037(02)01139-0

Maier CG, Kelley KK (1932) An equation for the representation of high-temperature heat content data1. J Am Chem Soc 54:3243. https://doi.org/10.1021/ja01347a029

Mauro JC, Yue Y, Ellison AJ et al (2009) Viscosity of glass-forming liquids. Proc Natl Acad Sci 106:19780–19784

Meerlender G (1974) Viskositäts-temperaturverhalten des standardglases I der DGG. Glas Ber 47:1–3

Moynihan CT (1993) Correlation between the width of the glass transition region and the temperature dependence of the viscosity of high-Tg glasses. J Am Ceram Soc 76:1081–1087. https://doi.org/10.1111/j.1151-2916.1993.tb03724.x

Moynihan CT (1995) Structural relaxation and the glass transition. Rev Miner 32:1–19

Moynihan CT, Easteal AJ, De Bolt MA, Tucker J (1976) Dependence of the fictive temperature of glass on cooling rate. J Am Ceram Soc 59:12–16

Moynihan CT, Lee S-K, Tatsumisago M, Minami T (1996) Estimation of activation energies for structural relaxation and viscous flow from DTA and DSC experiments. Thermochim Acta 280:153–162

Narayanaswamy O (1971) A model of structural relaxation in glass. J Am Ceram Soc 54:491–498

Narayanaswamy OS (1988) Thermorheological simplicity in the glass transition. J Am Ceram Soc 71:900–904

Nichols ARL, Potuzak M, Dingwell DB (2009) Cooling rates of basaltic hyaloclastites and pillow lava glasses from the HSDP2 drill core. Geochim Cosmochim Acta 73:1052–1066. https://doi.org/10.1016/j.gca.2008.11.023

Potuzak M, Nichols ARL, Dingwell DB, Clague DA (2008) Hyperquenched volcanic glass from Loihi Seamount. Hawaii Earth Planet Sci Lett 270:54–62. https://doi.org/10.1016/j.epsl.2008.03.018

Quane SL, Russell JK, Friedlander EA (2009) Time scales of compaction in volcanic systems. Geology 37:471–474. https://doi.org/10.1130/G25625A.1

Reinsch S, Nascimento MLF, Müller R, Zanotto ED (2008) Crystal growth kinetics in cordierite and diopside glasses in wide temperature ranges. J Non Cryst Solids 354:5386–5394. https://doi.org/10.1016/j.jnoncrysol.2008.09.007

Richet P, Lejeune AM, Holtz F, Roux J (1996) Water and the viscosity of andesite melts. Chem Geol 128:185–197. https://doi.org/10.1016/0009-2541(95)00172-7

Russell JK, Giordano D, Dingwell DB (2003) High-temperature limits on viscosity of non-Arrhenian silicate melts. Am Mineral 88:1390–1394

Schawe JEK, Hess KU (2019) The kinetics of the glass transition of silicate glass measured by fast scanning calorimetry. Thermochim Acta 677:85–90. https://doi.org/10.1016/j.tca.2019.01.001

Schawe JEK, Pogatscher S (2016) Material characterization by fast scanning calorimetry: practice and applications. In: Schick C, Mathot V (eds) Fast scanning calorimetry. Springer, Berlin, pp 3–80. https://doi.org/10.1007/978-3-319-31329-0

Scherer GW (1984) Use of the Adam-Gibbs equation in the analysis of structural relaxation. J Am Ceram Soc 67:504–511

Schott (2015) N-PK52A, 266-046–0, 2015. https://www.schott.com/d/advanced_optics/b5ef8322-fb8a-40ad-ae1b-5e8912087f1a/N-PK52A_SDS_EN_V5_201505.pdf?tenant=ao-cert

Shea T, Houghton BF, Gurioli L et al (2010) Textural studies of vesicles in volcanic rocks: An integrated methodology. J Volcanol Geotherm Res 190:271–289. https://doi.org/10.1016/j.jvolgeores.2009.12.003

Stabile P, Sicola S, Giuli G et al (2021) The effect of iron and alkali on the nanocrystal-free viscosity of volcanic melts: a combined Raman spectroscopy and DSC study. Chem Geol 559:119991. https://doi.org/10.1016/j.chemgeo.2020.119991

Tammann G, Hesse W (1926) Die Abhängigkeit der Viscosität von der Temperatur bie unterkühlten Flüssigkeiten. Zeitschrift Für Anorg Und Allg Chemie 156:245–257. https://doi.org/10.1002/zaac.19261560121

Tool AQ (1946) Relation between inelastic deformability and thermal expansion of glass in its annealing range. J Am Ceram Soc 29:240–253

Tool AQ, Eichlin CG (1931) Variations caused in the heating curves of glass by heat treatment. J Am Ceram Soc 14:276–308

Vasseur J, Wadsworth FB, Lavallée Y et al (2013) Volcanic sintering: timescales of viscous densification and strength recovery. Geophys Res Lett 40:5658–5664. https://doi.org/10.1002/2013GL058105

Vetere F, Iezzi G, Behrens H et al (2015) Glass forming ability and crystallisation behaviour of sub-alkaline silicate melts. Earth-Science Rev 150:25–44. https://doi.org/10.1016/j.earscirev.2015.07.001

Vogel H (1921) Das temperaturabhängigkeitsgesetz der viskosität von flüssigkeiten. Phys Z 22:645–646

Wadsworth FB, Vasseur J, Schauroth J et al (2019) A general model for welding of ash particles in volcanic systems validated using in situ X-ray tomography. Earth Planet Sci Lett 525:115726. https://doi.org/10.1016/j.epsl.2019.115726

Webb SL (2021) Thermal stress, cooling-rate and fictive temperature of silicate melts. Contrib Miner Pet 176:1–9. https://doi.org/10.1007/s00410-021-01836-y

Webb SL, Knoche R, Dingwell DB (1992) Determination of silicate liquid thermal expansivity using dilatometry and calorimetry. Eur J Mineral 4:95–104

Wilding MC, Webb SL, Dingwell DB (1995) Evaluation of a relaxation geospeedometer for volcanic glasses. Chem Geol 125:137–148. https://doi.org/10.1016/0009-2541(95)00067-V

Wilding MC, Webb SL, Dingwell DB (1996a) Tektite cooling rates: caolorimetric relaxation geospeedometry applied to a natural glass. Geochim Cosmochim Acta 60:1099–1103

Wilding MC, Webb SL, Dingwell DB et al (1996b) Cooling rate variation in natural volcanic glasses from Tenerife, Canary Islands. Contrib Miner Pet 125:151–160. https://doi.org/10.1007/s004100050212

Wilding MC, Dingwell DB, Batiza R, Wilson L (2000) Cooling rates of hyaloclastites: applications of relaxation geospeedometry to undersea volcanic deposits. Bull Volcanol 61:527–536. https://doi.org/10.1007/s004450050003

Wilding MC, Smellie JL, Morgan S et al (2004) Cooling process recorded in subglacially erupted rhyolite glasses: rapid quenching, thermal buffering, and the formation of meltwater. J Geophys Res Solid Earth 109:1–13. https://doi.org/10.1029/2003JB002721

Yue YZ, Christiansen JD, Jensen SL (2002) Determination of the fictive temperature for a hyperquenched glass. Chem Phys Lett 357:20–24. https://doi.org/10.1016/S0009-2614(02)00434-7

Yue Y, der Ohe R, Jensen SL (2004) Fictive temperature, cooling rate, and viscosity of glasses. J Chem Phys 120:8053–8059. https://doi.org/10.1063/1.1689951

Zhang Y, Jenkins J, Xu Z (1997) Kinetics of the reaction $H_2O + O \leftrightarrow 2OH$ in rhyolitic glasses upon cooling: geospeedometry and comparison with glass transition. Geochim Cosmochim Acta 61:2167–2173

Zhang Y, Xu Z, Behrens H (2000) Hydrous species geospeedometer in rhyolite: improved calibration and application. Geochim Cosmochim Acta 64:3347–3355. https://doi.org/10.1016/S0016-7037(00)00424-5

Zheng Q, Mauro JC, Yue Y (2017) Reconciling calorimetric and kinetic fragilities of glass-forming liquids. J Non Cryst Solids 456:95–100

Zheng Q, Zhang Y, Montazerian M et al (2019) Understanding glass through differential scanning calorimetry. Chem Rev 119:7848–7939. https://doi.org/10.1021/acs.chemrev.8b00510